Journal of the Mechanical Behavior of Biomedical Materials 167 (2025) 106966

Contents lists available at ScienceDirect

Journal of the Mechanical Behavior of Biomedical Materials

journal homepage: www.elsevier.com/locate/jmbbm

Bone mechanical behavior around dental implants: Densification and deformation follow-up by *in-situ* computed tomography

Laura Preiss [a,*], Rémy Gauthier [a], Hervé Richard [b], Loïc Courtois [c], Anne-Lise Chopard-Lallier [b], Damien Fabrègue [a], Jérôme Chevalier [a], Nicolas Courtois [b]

[a] Univ Lyon, INSA Lyon, UCBL, CNRS, MATEIS, UMR5510, 20 Avenue Albert Einstein, Villeurbanne, 69621, France
[b] Anthogyr SAS, 2237 Avenue A. Lasquin, 74700, Sallanches, France
[c] 3Dmagination, Harwell, United Kingdom

ARTICLE INFO

Keywords:
Bone densification
Dental implants
Strain distribution
High-resolution X-ray tomography
Peri-Implant bone
Primary stability
Digital volume correlation

ABSTRACT

The state of bone tissue around dental implants is a crucial factor influencing their early clinical outcomes. Currently, this state is mainly defined by its primary stability, both in terms of biomechanical analysis and clinically. The clinical methods used for quantifying this stability—such as the Implant Stability Quotient (ISQ) and Insertion Torque (IT)—are indirect measures. While these methods provide insights into the overall mechanical behavior of the bone-implant system, they do not account for the impact of implant morphology on the surrounding bone. The method presented here aims to analyze the peri-implant bone using image analysis and volume correlation techniques combined with computed tomography to assess the bone strain field and densification resulting from dental implant placement. The study utilized two types of implants with distinct designs—one cylindrical and the other self-tapping—on five iliac crest bone samples harvested from butcher pigs. The results indicated that the self-tapping implant caused significantly greater bone densification near the implant compared to the cylindrical one (46% of densification in the first 30 μm, against 21% for cylindrical implant). Additionally, the volume of strained peri-implant bone appeared to be larger for the self-tapping implant (38% of the volume was mechanically affected above 0,5% VM strains for self-tapping implant, against 31% for the cylindrical implant), though this difference was not statistically significant. Furthermore, established descriptors from the literature struggled to effectively differentiate between the two implant types. Despite the study's limitations, the proposed method shows promise for distinguishing implants based on the densification and deformation of peri-implant bone, and can serve as a complementary approach to standard ISQ and IT measurements.

1. Introduction

The success of dental implant surgery relies on the establishment of a strong and direct link between the implant's outer surface and the surrounding bone, the so-called osseointegration (Brånemark et al., 1970). Osseointegration is the result of a biological process, including healing and remodeling mechanisms, taking place from implantation until a few months (Albrektsson and Johansson, 2001). Osseointegration is influenced by the inflammatory and immunological host response (Berglundh et al., 1994), the implant surface (Buser et al., 1991), and also by primary stability (Schwarz et al., 2007). In the early time of bone healing at the implant/bone interface, micromotions allowed by a low primary stability may limit the implant anchorage (Kohli et al., 2021; Moncler et al., 1997; Prendergast et al., 1997) and would be deleterious for bone healing and the further implant long terms stability (Chou and Müftü, 2013).

Although bone healing has been extensively studied (Davies, 1996, 2003) and quantitative measurement techniques like histomorphometry consensually established, indicators of implant primary stability (periotest, insertion torque, Implant Stability Quotient - ISQ) (Al-Jetaily & Al-dosari, 2011; Atsumi et al., 2007; Meredith, 1998) are macroscopic and do not provide precise information on the local bone-implant interaction. Primary stability determined by insertion torque is highly intuitive and clinically accessible but is dependent of the implant external geometry and osteotomy size. In terms of biomechanics, an implant is considered to have primary stability if micromotions are

* Corresponding author.
E-mail address: laura.preiss@insa-lyon.fr (L. Preiss).

https://doi.org/10.1016/j.jmbbm.2025.106966
Received 29 October 2024; Received in revised form 14 February 2025; Accepted 1 March 2025
Available online 6 March 2025

minimized at the bone-implant interface.

The peri-implant strain developed during implant placement is believed to influence this primary stability. For instance, it was shown that the force applied perpendicularly to the implant during implant press fitting procedure contributed to implant primary stability (Damm et al., 2017). Moreover, peri-implant tissue strain state will have an influence on its further mechanobiological response. In the context of dental implant, while the influence of an axial loading on the development of peri-implant strain is largely studied (Dantas et al., 2020; Du et al., 2015; Park et al., 2022; Wili et al., 2024; Zhou et al., 2020) there are still few studies on the influence of implant insertion on strain distribution (Sotto-Maior et al., 2010; Udomsawat et al., 2019; Yang et al., 2023). Moreover, while two of these studies are only based on numerical analyses (Sotto-Maior et al., 2010; Udomsawat et al., 2019), the last relies on digital image correlation, that corresponds to a 2D analysis (Yang et al., 2023). This might be explained by the lack of an experimental pipeline to follow bone architecture modification before and after the insertion of the implant.

In addition, peri-implant bone densification is also assumed to contribute to peri-implant bone healing (Apelt et al., 2004; Guillaume et al., 2021; He et al., 2017; Le Cann et al., 2019; Trisi et al., 2009) and to promote faster osseointegration (Huwais and Meyer, 2017; Lahens et al., 2016; Lopez et al., 2017; Trisi et al., 2016). In the present work, osseodensification is defined as the competition between trabecular bone fragments formation and local trabecular compaction close to the implant surface, in trabecular region. The influence of such peri-implant densification on the implant primary stability is currently still discussed and might depend on the initial bone volume fraction (Almutairi et al., 2018; Fanali et al., 2021; Padhye et al., 2020). The influence of osseodensification around implants on the primary stability has already been investigated recently (Almutairi et al., 2018; Ferreira et al., 2023; Walid et al., 2019). While such densification was associated with a higher implant stability when inserted in polyurethane blocks (Fanali et al., 2021), a densification did not improve the implant stability in *ex vivo* bone samples, especially for good bone quality (Almutairi et al., 2018; Ferreira et al., 2023). In these previous studies investigating the influence of osseodensification on implant stability, the evaluation of the peri-implant densification is mainly performed through 2D histological sections (Padhye et al., 2020). These results suggest that not only primary stability is involved in the biological evolution of peri-implant bone. In 3D, bone densification around dental implants has been documented through microtomography but not precisely quantified (Fontes Pereira et al., 2023). Furthermore, conventional dental X-Ray imaging techniques lack the necessary resolution to accurately assess bone transformation close to the implant. To counter these constraints, high-resolution X-Ray computed tomography is generally used to investigate small scale features of dental implants and/or bone (Steiner et al., 2016). Accordingly, Ferreira et al. recently investigated the variation of bone volume fraction around an osteotomy applied through different methodologies (Ferreira et al., 2023). While this study showed different mechanisms of densification during osteotomy, no data were provided regarding trabecular bone densification after implant insertion.

To better understand how such osseodensification, in complement to primary stability, can improve dental implant early outcomes, it seems relevant to investigate the mechanisms of densification and its influence on bone behavior during the implant insertion in 3D. This work thus presents a novel *ex vivo* method based on high resolution X-Ray tomography to quantitatively assess bone densification and locally induced strains associated to dental implant insertion. This new method enables *in situ* monitoring of these two parameters during the implantation.

2. Materials and methods

2.1. Model selection and samples preparation

2.1.1. Bone samples

Samples were taken from farm pig carcasses within 24–48 h of slaughter. The samples were cut in 12 × 12 mm^2 prism shape from pig pelvis (ischium), chosen for its similarity with human jawbone and reliability in new implant design evaluation (Katranji et al., 2007; Merheb et al., 2010; Pearce et al., 2007; Porto et al., 2020). They were directly wrapped in Parafilm M®(Bemis Company Inc., USA) and stored at −18 °C to prevent bone degradation awaiting the embedding day. Bone samples were removed from the freezer and placed in the holder for embedding in polyurethane and stored again at −18 °C until the day of testing (see Fig. 1).

2.1.2. Dental implants

Two types of dental implants with different thread designs and insertion protocols were used. Implant A (Axiom® REG, Anthogyr, Sallanches, France) was a cylindrical implant supposed to be placed with extensive bone preparation while implant B (Axiom X3®, Anthogyr, Sallanches, France) was self-tapping, with sharp threads designed to cut the bone and anchor after minimal preparation (Fig. 2).

2.2. In situ implantation

2.2.1. Experimental set up

A picture of the testing jig is shown in Fig. 3. The setup was designed for reproducible site preparation and implant insertion. Vertical guides maintained a constant alignment between the site preparation tools, implant and osteotomy while the mass fixed below the contra-angle (100 g) ensured an engagement load for implant insertion similar to clinical conditions. Tests were carried out using the GE Phoenix v|tome|x tomograph (GE Sensing & Inspection Technologies Phoenix X|ray, Pforzheim, Germany). The scan parameters were as follows: tension of 140 kV, current of 80 μA, 2400 projections, 500 ms of exposure time, copper filter 100 μm, voxel size 12x12x12 μm^3.

2.2.2. Protocol

a. Bone samples selection

To allow for comparison, bone samples were selected based on their morphological criteria, *i.e.* bone volume fraction (BV/TV)/homogeneity/height.

For all samples, 3 scans were acquired: one of the ‘intact’, one of the ‘pre-implant’ bone, after the first steps of drilling (see implantation protocol below) in which the osteotomy was filled with a Titanium pin and one of the ‘post-implant’ bone (performed after the implant insertion). The titanium pin was inserted into the implant site to replicate the artifacts caused by the contrast difference between titanium and bone, which will appear in the ‘post-implant’ scans (see ‘tomography protocol’ section). All three datasets were first registered to align undamaged bone within a sub-voxel accuracy (see Fig. 4).

After first applying a ‘non-local means’ filter (Gastal and Oliveiray, 2012) to the ‘intact’ bone scans, an automatic thresholding algorithm (Otsu, 1979) was applied to obtain a binary map of bone. A local volume fraction of bone was then measured at each voxel location using a spherical kernel of size 100 voxels (ratio of ‘bone’ voxels divided by the total number of voxels). The resulting local bone volume fraction map, shown in Fig. 5-c, gives insight into the heterogeneous distribution of trabeculae throughout the bone sample as well as the bone characteristics at the implant location.

Additionally, a local thickness (Hildebrand and Rüegsegger, 1997) of the binary bone map was measured around the location of the drilled hole (6 mm by 6 mm region centered around the implant axis).

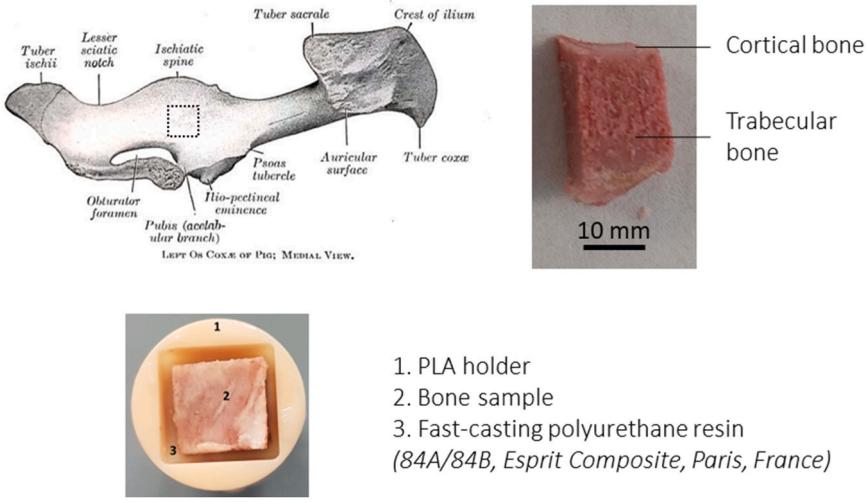

Fig. 1. *Top left: Pig hip with sampling site* (Mishra, 2020). *Top right: bone sample after cutting and before embedding. Bottom: samples in the holder, here before impregnation in resin.*

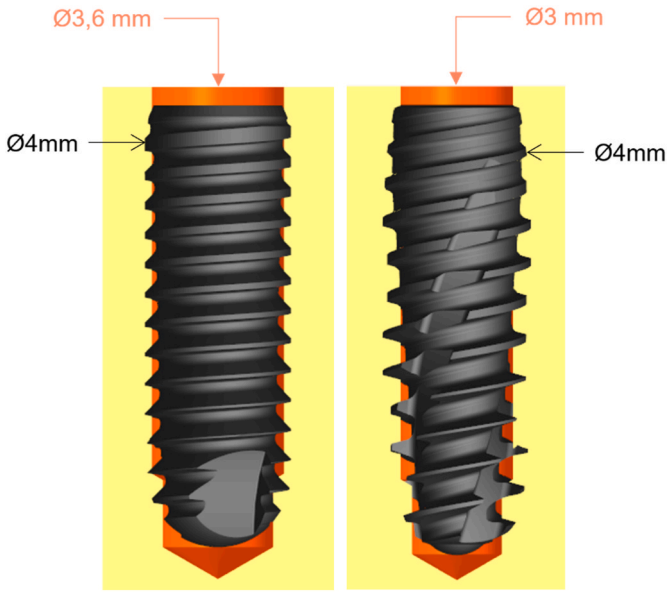

Fig. 2. Schematics of implants in their osteotomy sites (left: implant A, right: implant B).

Trabeculae were filtered out, based on their thickness, in order to isolate the cortical bone region. As a result, a distribution and average of the cortical bone thickness could be measured (see Fig. 5-b) for each bone sample.

Samples homogeneity was first characterized by fast observations of the 3D volumes: samples with large pores (over 500 µm in diameter) were discarded. In terms of height, only bone samples in which insertion of a 12 mm long implant was possible were selected. A cortical thickness of around 1 mm is recommended, to be as close as possible to the human jawbone (Katranji et al., 2007). An effort was thus made to closely approach this objective, despite the available bones having variable cortical thicknesses.

As a result of these calculations/observations, 10 samples were chosen. Their characteristics are gathered in Table 1. Bones A1 to A5 were implanted with dental implant A, while bones B1 to B5 were implanted with implant B.

b. Implantation protocol

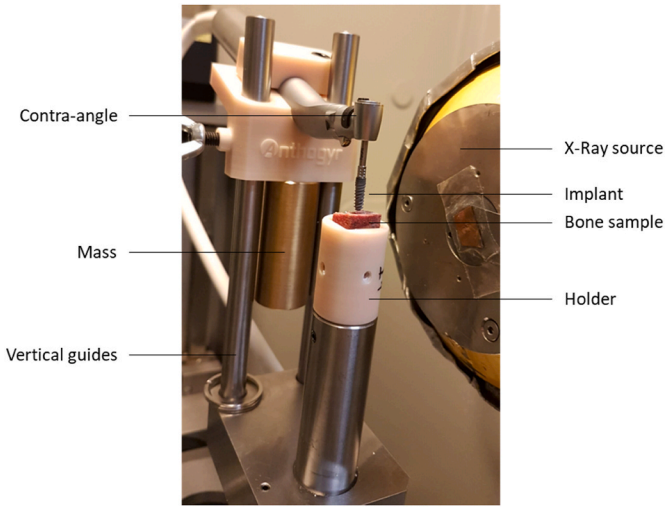

Fig. 3. Tomography setup description.

Drilling was performed following the clinical instructions: first drill with a diameter of 2 mm at 1500 rpm, then successively 2.4 mm, and 3 mm (plus 3.6 mm for implant A) of diameter at 1000 rpm; using a dental contra-angle handpiece (ref 11750MLED). The depth of the implant hole corresponded to the length of the implant (in this case 10 mm and 12 mm) plus 0.5 mm so that in the end the implant is placed in the clinically 'sub crestal' suitable position, 0.5 mm underneath the surface. The hole's diameter depended on the protocol used (3.6 mm for implant A, 3 mm for implant B). This corresponds to the 'pre-implant' state. The implantation protocol for implants A and B was different: with an equivalent protocol, the diameter of the implantation pit was closer to the implant diameter for implant A (Fig. 2). This resulted in a more self-tapping implant B.

c. Tomography protocol

The first stage of tomography was the 'intact' bone for bone parameters evaluation. Then, the 'pre-implant' volume was acquired. This step was essential because it allowed to access to the deformation field and densification state of the bone around the implant through image processing and volume correlation. It can be noticed that the implant well did not remain empty during this tomography. Indeed, it is known

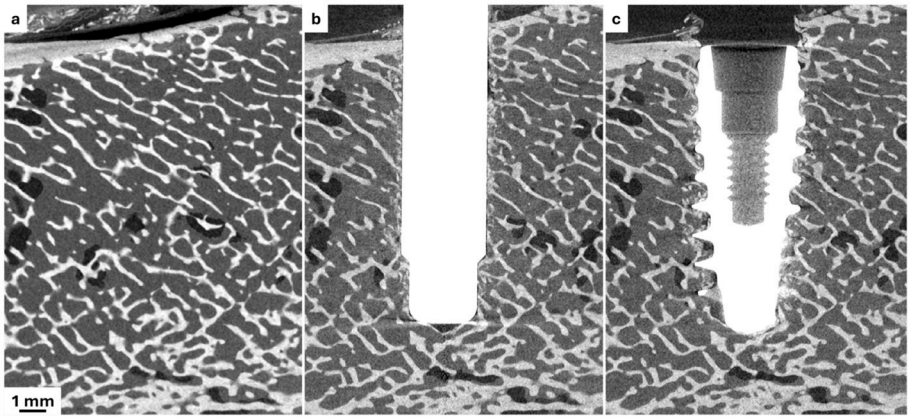

Fig. 4. Grayscale slice of a) 'intact' bone, b) 'pre-implant' bone and pin, and c) 'post-implant' bone.

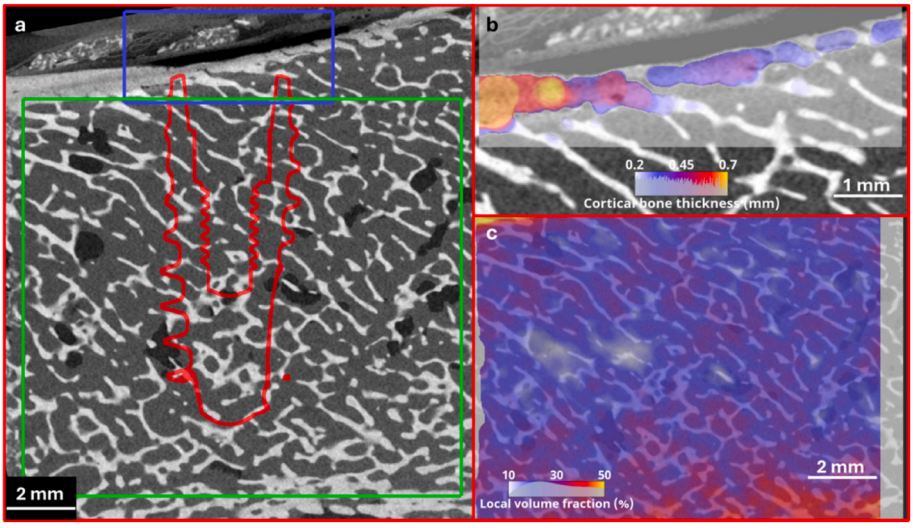

Fig. 5. a) Grayscale cross-section showing the 'intact' data, b) Cortical bone thickness measurement shown on the 'blue region' shown on a), c) Local volume fraction measurement shown in the 'green region' shown on a).

Table 1
Cortical thickness, d10 and bone volume fraction before and after implant insertion (average over 2 mm around the implant) for each bone sample. *: significant difference between implant A and B (p-value <0.05).

	Bone sample	$BVTV_{before\ insertion}$ (%)	$BVTV_{after\ insertion}$ (%)	Cortical thickness (mm)	IT (N. cm)	d_{10} (μm)
Implant A	A1	27	30	1.12	51	111
	A2	31	30	1.00	58	61
	A3	30	29	0.89	56	100
	A4	26	29	0.55	42	70
	A5	30	34	0.86	68	106
	Average	**29**	**31**	**0.88***	**55**	**90***
	SD	2	2	0.20	9	20
Implant B	B1	25	29	0.40	41	292
	B2	26	35	0.81	80	220
	B3	39	46	0.39	80	401
	B4	32	38	0.29	51	443
	B5	33	38	0.30	58	434
	Average	**31**	**37**	**0.44***	**62**	**358***
	SD	6	6	0.20	17	87

that during the tomography of titanium implants placed in the bone, artifacts due to the differences in attenuation between titanium and bone appear. To reproduce these artifacts and limit disturbance during the DVC measurements, a cylindrical titanium 'decoy' (or pin) was thus inserted into the well during the 'pre-implant' scan.

Once the 'pre-implant' scan was performed, the insertion of the implant into the scanner, under the beam, was conducted. The rotation of the stage was deactivated, so that the insertion of the implant was filmed in 2D radiography during the entire descent of the implant (acquisition rate 3 frame/s). One example of an insertion is given as supplementary material. The insertion was carried out at 15 rpm, according to the protocol instructions, with the aid of a dental contra-angle handpiece (see Fig. 3). Implants were placed and their insertion torque did not exceed 80 N cm as recommended.

The last step of the experiment was to perform a tomography under the same conditions as the 'pre-implant' volume to compare the bone properties before and after implantation ('post-implant' volume).

The whole protocol is summarized in Fig. 6.

2.3. Data processing

2.3.1. Implantation measurements

Based on the aligned pre ('pre-implant') and post ('post-implant') scans, a binary mask of the whole bone region surrounding the

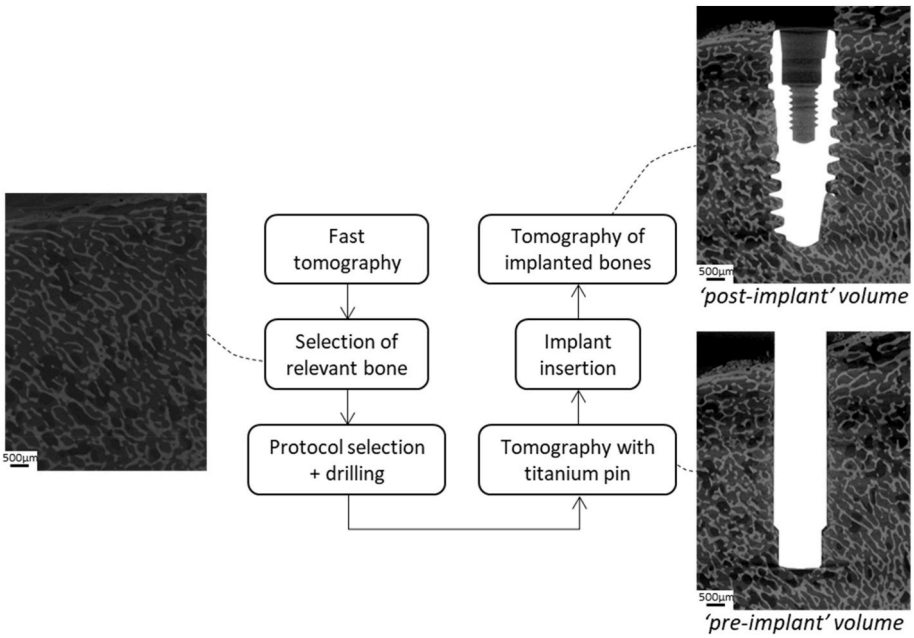

Fig. 6. Test protocol steps.

implantation zone was defined, excluding the cortical region and all bone beyond the implant tip (see Fig. 7-a).

After the implant insertion, the trabecular bone volume fraction ($BVTV_{after\ insertion}$, in %) around the implant was calculated on a volume of interest spreading 2 mm from the implant surface. This BV/TV was only measured on the trabecular region of the bone, the cortical layer was not considered. This represents a global picture of bone densification around the implant (Ferreira et al., 2023). Then, for all voxels belonging to this mask, an Euclidian distance map (see Fig. 7-a) was computed in which each voxel gets assigned a value corresponding to its closest distance to a free surface (here the hole/implant surface).

For increasing bins of 0.05 mm width (Fig. 7-b), an average grayscale value is measured for both the pre and post scans (see Fig. 7-c). Due to grayscale variations between scans (variation in titanium thickness leading to artifacts), the 'post' grayscale value was then corrected so that the value in the bulk of the bone, away from the implant (2 mm from implant surface) matches the 'pre' grayscale value (see Fig. 7-c). A densification percentage for each bin is calculated by comparing the post-implantation average grayscale value to the value corresponding to mineralized bone in the trabecular region. This reference value is defined as 110% of the peak grayscale value observed in the histogram, to account for the spread of the peak, on 'pre-implant' volume. Essentially, the densification is considered to be 100% if the post-implantation grayscale value reaches this reference.

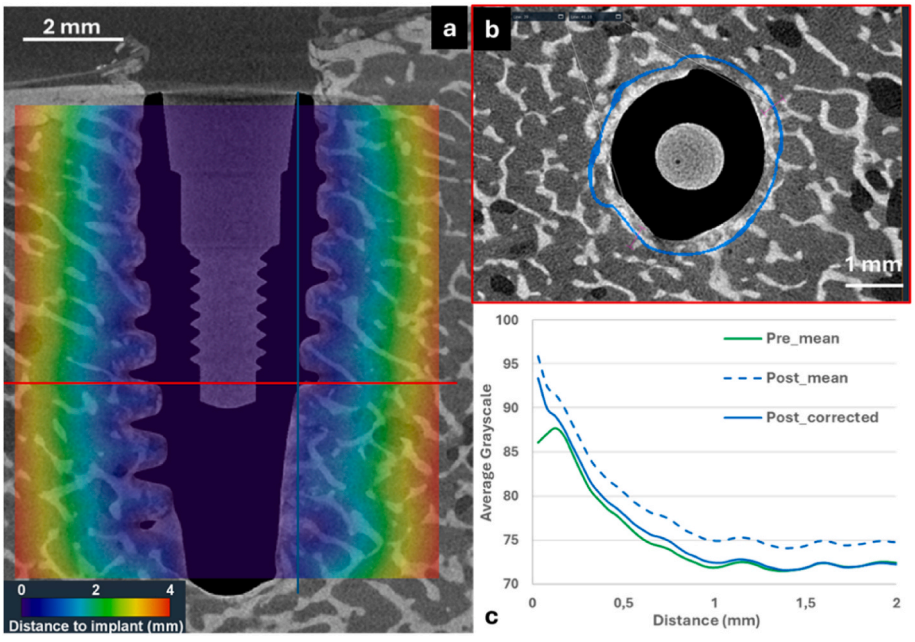

Fig. 7. a) Distance map, b) cross-section of a 0.05 mm bin in blue (positioned at the red line in Fig. 7-a), c) Average grayscale measured for 'pre' and 'post' scans as a function of the distance to the implant surface.

2.3.2. Volume correlation

The aligned pre and post grayscale datasets were also used to measure a 3D displacements field via Digital Volume Correlation (DVC). The approach used here for Volume Correlation is known as an FE-based Global approach, which also includes mechanical regularization (Roux et al., 2008; Taillandier-Thomas et al., 2014). Measurements were conducted using the XDigitalVolumeCorrelation extension to the Avizo software (version 2023.2).

A 3D tetrahedral mesh was first prepared, covering the full region on which the correlation will be performed. As the size of the elements constituting the mesh is closely related to the characteristic length-scale of the bone microstructure, a suitable element size for this mesh was defined by performing an uncertainty analysis on an undeformed portion of the trabecular bone region, taken from an intact bone scan and a 'pre-implant' scan, far away from the drilled hole. A zero strain study was performed for increasing sizes of the tetrahedral elements making up the mesh. Fig. 8-a shows a plot of both the displacement and corresponding strain uncertainty as a function of the edge length of the tetrahedral mesh. It was decided to aim for a displacement uncertainty around 0.1 voxel and so the element size was set to 40 voxels, with a mechanical regularization length set to twice the average element size (80 voxels). This resulted in a strain; Fig. 8-b shows the resulting mesh for sample B1.

The DVC computation then resulted in a displacement field at each node of the mesh and the Green-Lagrange strain tensor was computed. Finally, the volumetric strain and Von Mises equivalent strain were obtained (FEA manual guide, n.d.) and combined with geometric descriptors such as the normalized height along the implant (from 0% at the apex of the implant tip to 100% at the top of the implant) and the distance to the implant surface, as measured from the Euclidian distance map.

2.4. Statistical analysis

Due to the low number of samples, the difference in densification between implants A and B were evaluated by applying the non-parametric Mann-Whitney. Linear regressions were applied to measure correlation between bone morphological parameters and the IT and ISQ. These statistical tests were done using R software (The R Foundation for Statistical Computing, Austria). A p-value <0.05 was considered as significant.

3. Results

3.1. Bone initial characterization

Bone volume fraction, under the cortical layer, and cortical thickness for the different samples are reported in Table 1. The average bone volume fraction was 29% for samples A1 to A5 and 31% for B1 to B5, with no significant difference. The cortical thickness was on average 0.88 mm for A1 to A5 and 0.44 mm for B1 to B5 with a significant difference ($p = 0.01$).

3.2. Implant-related bone densification

The overall subcortical bone volume fraction in the peri-implant region, averaged within 2 mm thick VOI from the implant surface, is presented in Table 1 for both implant types. No statistical difference was found between implants A and B.

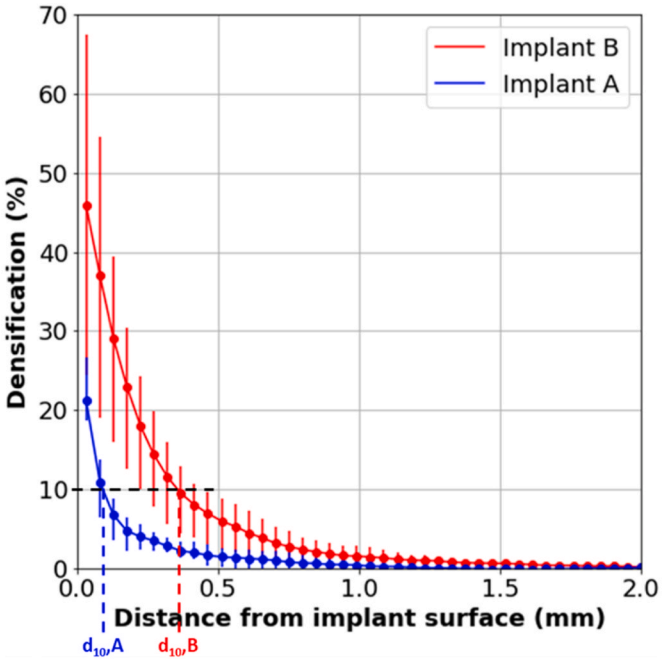

Fig. 9. densification ratio as function of distance to implant for each implant type (mean value with min and max envelope for each type of implants, N = 5).

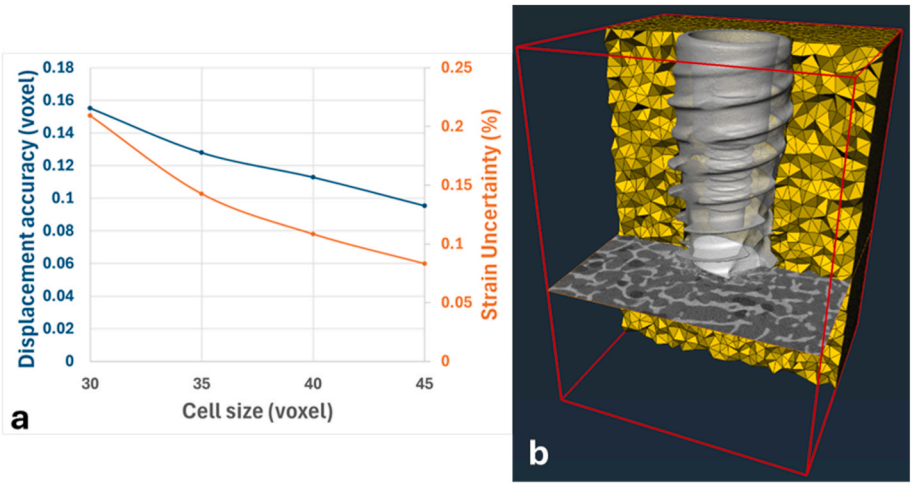

Fig. 8. a) Uncertainty plot, b) 3D Tetrahedral mesh (Yellow) defining the DVC computation region for sample B1.

The increase in the volume fraction of bone around the implants is an indicator of bone densification in trabecular area. From the pre- and post-implant CT scans, it was possible to calculate the bone densification as a function of the distance from the implant surface (Fig. 9). A high level of densification (>20%) was observed near the implant, gradually decreasing up to a distance of 1 mm from the implant surface.

The statistical analyses confirmed that the densification was significantly higher for the implant B up to 500 μm (~40 voxels) from the implant surface (Table 2). The differences were non-significant for distances larger than 600 μm.

Significant differences were measured between implants A and B in terms of densification, in particular close to the implant. To characterize this peri-implant bone densification, the d_{10} indicator was arbitrarily set, defined as the distance at which a densification ratio of 10% was measured. This indicator measures the capacity of an implant to increase the trabecular bone volume fraction in its vicinity (Table 1).

In relation to densification, bone debris were observed along the implant after its insertion (Fig. 10). Only debris disconnected from the trabecular network with a characteristic size exceeding 60 μm could be isolated through segmentation.

3.3. Bone deformation

3.3.1. Strain distribution

Volumetric strains were measured using DVC for each implant. Fig. 11 represents the volumetric deformations around each implant type. The implant was divided into four regions (from 0% to 100%, apex to neck), for which volumetric deformations were measured as a function of the distance (in 0.5 mm bins) from the implant, from the surface to a distance of 2.5 mm.

A compressive strain is observed near the implant, which gradually decreases to zero with increasing distance from the implant surface. This effect is more pronounced for implant B. Fig. 11 highlights a variation along the height of implant B, showing a higher compressive strain near the implant neck.

3.3.2. Affected volume

A 'mechanically-affected bone volume fraction' was determined by calculating the ratio of voxels with a Von Mises strain exceeding 0.5% to the total number of voxels within a 2.5 mm radius of the implant surface. The 0.5% threshold was chosen to be five times the uncertainty in the measurement of strains (0.1%), and still relevant of the bone strains levels recorded in the literature (Cowin, 2001). Fig. 12 shows the strain repartition along and around the implant for both types of implants.

Fig. 13 shows that the volume of bone affected was greater when implant B was inserted (38%), compared to implant A (31%). No significant difference was measured between implants A and B. However, with the exception of Sample A1, that had the largest mechanically-affected volume, implants B affected systematically a larger bone volume than implants A.

Table 2
Densification ratio (in %) calculated over increasing breadth around the implant. *: significant difference between implant A and B (p-value <0.05).

Distance to the implant (voxels)		2.5	22.5	42.5	62.5	82.5
Distance to the implant (μm)		30	270	510	750	990
	Bone sample	Densification ratio (%)				
Implant A	A1	19	5	2	1	1
	A2	19	2	0	0	0
	A3	21	3	1	0	0
	A4	20	3	2	2	1
	A5	27	4	1	1	1
	Average	**21***	**3***	**1***	1	0
	SD	3	1	1	1	1
Implant B	B1	47	11	4	1	0
	B2	24	8	2	1	1
	B3	41	17	7	2	2
	B4	49	16	9	4	2
	B5	68	20	8	5	3
	Average	**46***	**14***	**6***	3	1
	SD	14	4	3	2	1

3.4. Association with ISQ and insertion torque

For Implant A, the d_{10} indicator was relatively stable (61 μm < $d_{10,A}$ < 111 μm), whereas the insertion torque (IT) values varied considerably (42 N cm < IT_A < 68 N cm), and the ISQ remained between 66 and 73 (see Fig. 14). The volumetric fraction of mechanically affected bone ranged from 23.6% to 45.9%. For Implant B, the d_{10} ranged from 220 to 443 μm, the volumetric fraction of mechanically affected bone ranged from 31.6% to 42.8%, the insertion torque ranged from 41 to 80 N cm (with the contra-angle limited to 80 N cm, suggesting this value might have been underestimated), and the ISQ ranged from 48 to 79. Finally, a significant Pearson correlation was found between IT and $BVTV_{after\ insertion}$ ($r = 0.7$, p-value = 0.03), but not with the ISQ. By including both the cortical thickness and the $BVTV_{after\ insertion}$ in the linear regression, the correlation with IT was improved ($r = 0.8$, p-value = 0.008), No correlation was observed between cortical thickness and IT nor ISQ.

4. Discussion

4.1. Relevance of the method

Based on the literature, both peri-implant bone densification and deformation due to implant insertion are involved in peri-implant bone long term evolution and in the implant outcome. This study details a new micro-computed tomography driven method for evaluation of both bone densification and deformation that result from the placement of two morphologically distinct implants. This methodology permits robust measurements of bone response metrics compared to traditional methods (Saidin et al., 2012). Although peri-implant bone densification is suspected to improve the implant efficiency, particularly in low-density bones, standardized methods currently do not exist to quantify it. Previous studies evaluating the influence of osseodensification assessed densification by measuring the bone volume/area fraction around the implant (Ferreira et al., 2023; Padhye et al., 2020) independent of the initial bone quality. In the current study, the bone gray level after implant insertion is compared with the gray level before the insertion. In that way, this method is less sensitive to the initial bone density. Furthermore, the methodology allows an analysis as a function of the distance to the implant. For instance, the higher densification that is expected for a self-tapping implant design was quantified on implant B at different distance from its surface. The densification was still significantly higher for implant B compared to implant An up to 500 μm from the implant surface, with an averaged densification of 6% and 1% respectively. Such *in situ* characterization allows definition of new markers (such as the d_{10}) of the implant osseodensification considering both the bone volume fraction before and after the insertion and the distance to the implant. The markers Suggested in the current study were defined arbitrarily and their influence on the implant clinical outcomes need to be further validated through *in vivo* experimentations.

4.2. Densification and primary stability

Bone volume fraction was previously associated with an increased primary stability *ex vivo* (Padhye et al., 2020). Similarly, the current study also observed increased primary stability, as evidenced by the significant correlation between the bone volume fraction surrounding the implant (within a 2 mm distance from the implant surface) and the insertion torque. Although significant, it should be noted that the

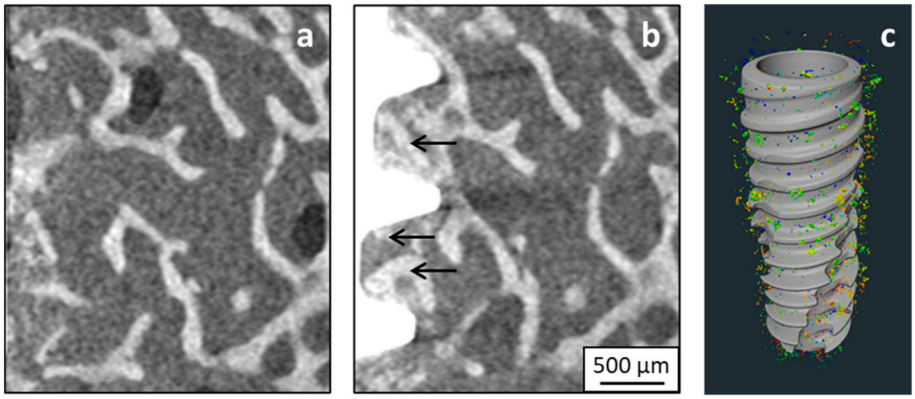

Fig. 10. example of bone fragments visualization for implant B. a: bone before implant insertion, b: bone after implant insertion, black arrows indicate isolated bone debris, c: 3D visualization of the debris repartition along the implant.

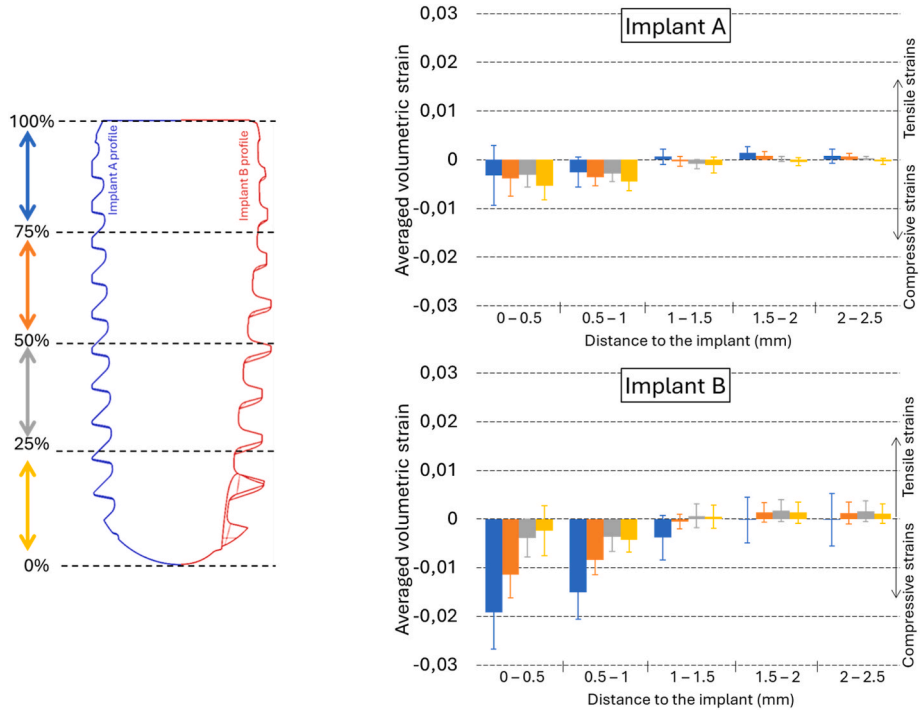

Fig. 11. left: implant division into four regions in height; right: volumetric strain repartition as a function of the distance to the implant (top: Implant A, bottom: Implant B).

correlation remains modest (r = 0.7), and no correlation was identified with the ISQ.

It was established that the primary stability of an implant is predominantly ensured by the cortical layer, even when of minimal thickness (Ruffoni et al., 2012). This result is in accordance with the significant correlation between IT and a combination between the $BVTV_{afterinsertion}$ and the cortical thickness, regardless of the implant geometry and considering that the cortical thickness was significantly different between the two sets of samples. On the other hand, no correlation with IT was observed when considering the d_{10}. This suggests that this last parameter is not involved in the implant primary stability as defined clinically. Still, while $BVTV_{after\ insertion}$ was not different between A and B implants, d_{10} can be used to distinguish the two kinds of implant. The volume of mechanically affected bone and strain distribution provided additional insights. Implant B induced a larger affected bone volume with higher strain levels, particularly near its neck, suggesting a potentially greater stress transfer to the surrounding bone compared to Implant A (He et al., 2017; Trisi et al., 2016). No significant difference was observed, mainly because implant A1 presented a higher volume fraction with strain higher than 0.5%. This may be due to the poor positioning of the implant in the osteotomy: the implant was placed too deeply, in contact with the cortical bone at its apex, which led to a large proportion of bone modified and affected in its vicinity (Fig. 15). Additionally, implant A1 presented the largest cortical thickness. A real trend can nevertheless be seen but must be confirmed by increasing the number of samples.

4.3. Clinical relevance

The bone strains measured in the current study can hardly be used to further estimate the bone healing and remodeling process occurring around the implant. To the author's knowledge, only few studies investigated the relationship between peri-implant strain induced by implant insertion and its primary stability (Hung et al., 2022; Yang et al., 2023). In these two previous *in silico* studies, increasing strains in the peri-implant tissue after insertion is associated with the implant

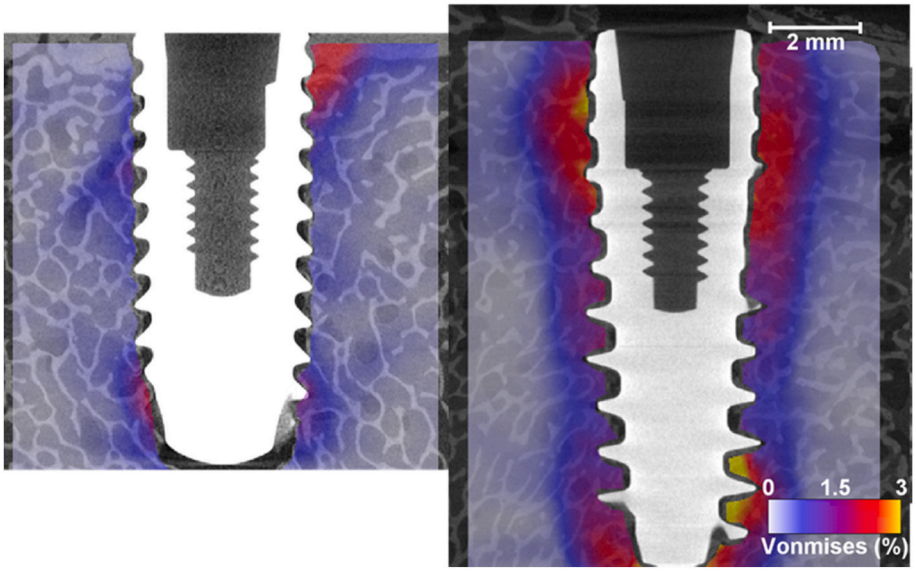

Fig. 12. Von Mises strains repartition around dental implants for implant A (left) and implant B (right).

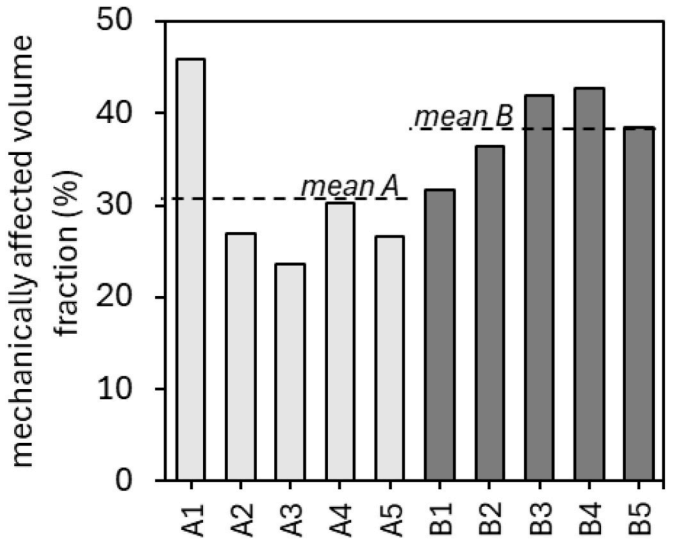

Fig. 13. Mechanically affected bone volume fraction (>0.5% VMstrain) for each bone; dashed lines: mean values per implant type.

insertion torque. Furthermore, one of them is focused on trabecular bone (Yang et al., 2023) and the other on cortical bone (Hung et al., 2022). In the current experimental study, no correlation was observed between the insertion torque and data on the peri-implant strain. The low number of samples and the different implant geometries investigated can be an explanation. Despite this, the new method enabled to differentiate two implant designs with regard to the strain induced in the bone during their insertion. Such peri-implant strain after the implant insertion represents a static deformation and might result in bone resorption (Lanyon and Rubin, 1985). However, it can be seen as a new initial condition for this peri-implant tissue that will then be loaded, for instance during mastication. This residual strain induced by implant insertion is never considered in numerical models of bone load-induced remodeling around a dental implant, while bone cells involved in this remodeling, such as the osteocytes that are closely trapped within the mineralized matrix, might be affected by this deformation (Verbruggen et al., 2012). The current method cannot predict further biological processes occurring around the implant, but it allows to characterize the initial strain state around the implant. Such data can be used and implemented in future numerical model of peri-implant remodeling. Besides the compaction of bone trabeculae during implant insertion, bone densification could be partly attributed to the presence of bone fragments around the implant. These debris added mineralized bone in empty regions, resulting in a local increase in the volume fraction of bone and thus densification. They were created during the drilling process and the insertion of the implant. The debris could either be pushed to the edges by the implant thread or resulted from trabeculae being broken by the thread itself during implant insertion, with the pieces then distributed around the implant (Fig. 10). In this study, several pieces of debris could be identified, but due to artifacts caused by the high attenuation of titanium compared to bone, it was difficult to accurately segment them. Overall, only the largest fragments (over 60 μm in diameter) could be detected, and only if they did not touch the trabecular network (Fig. 10-c). It has been suggested that bone fragments formed around an implant might promote bone formation (Shah and Palmquist, 2017). Depending on the size of such fragments, the osteocytes trapped with the mineralized matrix may have the capacity to communicate with the environment surrounding the bone fragments to promote new bone formation and repair the disrupted canaliculi by forming new connections with the new formed bone. However, the role of osteocytes in such bone healing process still needs to be further investigated. In the current study, the applied methodology allowed to observe some of these bone fragments around the bone. However the current spatial resolution did not allow to perform a rigorous morphological analysis of these fragments. Further evaluation involving higher spatial resolution techniques will hence be performed.

The methodology described in the current study has been developed to provide additional indicators of the bone-implant mechanical interactions during *in vitro* studies to help optimizing dental implants regardless of the bone quality. In this regard, the method allows to measure the densification ratio as a function of the distance to the implant surface, that is the ratio between the bone volume faction before and after the implant insertion. This indicator has been able to differentiate a cylindrical implant (A) from a self-tapping implant (B) with a low number of samples. In addition, the volume fraction of peri-implant bone with a von Mises strain higher than 0.5% was determined as a complementary indicator, because of the known influence of strain on bone mechanobiology. While this latter indicator did not allow to statistically differentiate implant A from implant B, a real tendency was obtained and will be further validated using higher resolution imaging

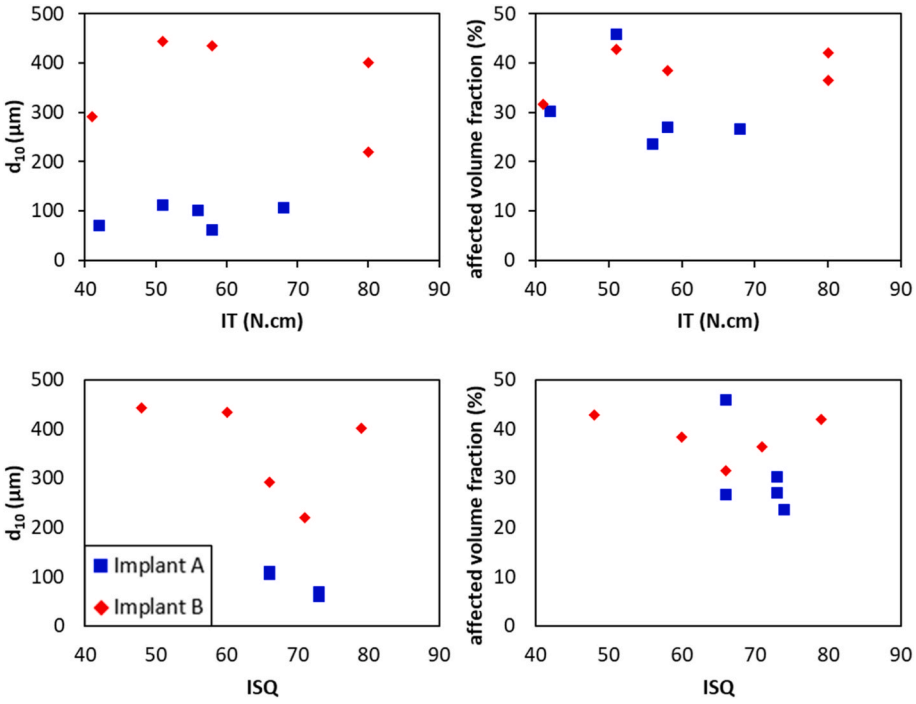

Fig. 14. comparison between new indicators and commonly used indicators of primary stability (left: bone densification vs IT (top) and vs ISQ (bottom), right: mechanically affected volume vs IT (top), and vs ISQ (bottom)).

techniques. These new indicators can be used in complement to some standard characterization techniques, such as the IT or the ISQ, that were not able to differentiate the implants in this study. A perspective of this work could be the use of this new method to assess the effect of dental implant design and surgical protocols on the surrounding bone and serve as a reliable baseline measurement of the initial biomechanical stimuli for later *in vivo* comparison.

While the study provides valuable data on bone-implant interactions, it is important to acknowledge its limitations.

4.4. Limitations

The use of porcine bone, while partly similar to human jawbone, may not perfectly replicate human bone behavior, although this model is used in new implant designs evaluation (Pearce et al., 2007). Various models have been used in the assessment of biomechanical incidence of dental implant insertion into bone (Bryant, 1998; Holmes and Loftus, 1997; Isidor, 2006; Sevimay et al., 2005). Synthetic polyurethane foam blocks (Sawbones, Vashon WA, USA) are commonly used in bench testing to evaluate surgical protocols. Photoelastic materials have also been used for comparative analyses of the stresses developed around various screw designs (Celik and Uludag, 2007; Dragoni, 1994; Goiato et al., 2009; Haraldson, 1980; Turcio et al., 2009).These models however are not relevant to assess the structural modifications of bone induced by implant insertion nor the stress state obtained after these modifications.

Additionally, the *in vitro* nature of the study does not account for biological factors such as the immune response and bone remodeling dynamics in a living organism. Future studies aim to validate these findings in clinical settings and explore the long-term effects of different implant designs on bone osseodensification, strain distribution, health and stability.

Finally, the relatively poor time and spatial resolution, together with the shadowing of titanium did not allow to observe the phenomena close to the implant during the insertion. Better spatial and time resolution, such as synchrotron-radiation based micro-computed tomography, could allow to investigate bone behavior close to the implant during its placement.

5. Conclusion

Osseodensification and peri-implant bone deformation distribution are known to be clinically relevant in the field of dental implantology. In the current study, we developed a methodology based on *in situ* micro-computed tomography of a bone sample during dental implant insertion. The surrounding bone densification and deformation, measured comparing bone before and after the implant insertion, was used to distinguish two types of implants with different geometries, while no difference was found using conventional characterizations (insertion torque or ISQ). In conclusion, the new method presented appears as a complementary characterization method in order to evaluate the influence of a geometry on the surrounding bone behavior that can be used for the development of new dental implants.

CRediT authorship contribution statement

Laura Preiss: Writing – original draft, Project administration, Methodology, Investigation, Formal analysis, Data curation, Conceptualization. **Rémy Gauthier:** Writing – original draft, Validation, Formal analysis. **Hervé Richard:** Methodology. **Loïc Courtois:** Writing – original draft, Methodology, Data curation. **Anne-Lise Chopard-Lallier:** Writing – review & editing, Supervision. **Damien Fabrègue:** Supervision. **Jérôme Chevalier:** Writing – review & editing, Supervision. **Nicolas Courtois:** Writing – review & editing, Supervision.

Declaration of competing interest

The authors declare that they have no known competing financial interests or personal relationships that could have appeared to influence the work reported in this paper.

Acknowledgements

The authors would like to thank J.Adrien for his help and support.

Appendix A. Supplementary data

Supplementary data to this article can be found online at https://doi.org/10.1016/j.jmbbm.2025.106966.

Data availability

Data will be made available on request.

References

Al-Jetaily, S., Al-dosari, A.A.F., 2011. Assessment of Osstell™ and Periotest® systems in measuring dental implant stability (in vitro study). Saudi Dental Journal 23 (1), 17–21. https://doi.org/10.1016/j.sdentj.2010.09.003.

Albrektsson, T., Johansson, C., 2001. Osteoinduction, osteoconduction and osseointegration. Eur. Spine J. 10, S96–S101. https://doi.org/10.1007/s005860100282.

Almutairi, A.S., Walid, M.A., Alkhodary, M.A., 2018. The effect of osseodensification and different thread designs on the dental implant primary stability. F1000Research 7, 1–10. https://doi.org/10.12688/f1000research.17292.1.

Apelt, D., Theiss, F., El-Warrak, A.O., Zlinszky, K., Bettschart-Wolfisberger, R., Bohner, M., Matter, S., Auer, J.A., Von Rechenberg, B., 2004. In vivo behavior of three different injectable hydraulic calcium phosphate cements. Biomaterials 25 (7–8), 1439–1451. https://doi.org/10.1016/j.biomaterials.2003.08.073.

Atsumi, M., Park, S., Wang, H.-L., 2007. Methods used to assess implant stability: current status. Int. J. Oral Maxillofac. Implants 22 (5).

Berglundh, T., Lindhe, J., Jonsson, K., Ericsson, I., 1994. The topography of the vascular systems in the periodontal and peri-implant tissues in the dog. J. Clin. Periodontol. 21 (3), 189–193. https://doi.org/10.1111/j.1600-051X.1994.tb00302.x.

Brånemark, P.I., Adell, R., Hansson, B.O., Breine, U., 1970. Intra-osseous anchorage of dental prostheses. Scand. J. Plast. ReConstr. Surg. Hand Surg. 4 (1), 19–34. https://doi.org/10.3109/02844317009038440.

Bryant, S.R., 1998. The effects of age, jaw site, and bone condition on oral implant outcomes. Int. J. Prosthodont. (IJP) 11 (5), 470–490.

Buser, D., Schenk, R.K., Steinemann, S., Fiorellini, J.P., Fox, C.H., Stich, H., 1991. Influence of surface characteristics on bone integration of titanium implants. A histomorphometric study in miniature pigs. J. Biomed. Mater. Res. 25 (7), 889–902. https://doi.org/10.1002/jbm.820250708.

Celik, G., Uludag, B., 2007. Photoelastic stress analysis of various retention mechanisms on 3-implant-retained mandibular overdentures. J. Prosthet. Dent 97 (4), 229–235. https://doi.org/10.1016/j.prosdent.2007.02.006.

Chou, H.Y., Müftü, S., 2013. Simulation of peri-implant bone healing due to immediate loading in dental implant treatments. J. Biomech. 46 (5), 871–878. https://doi.org/10.1016/j.jbiomech.2012.12.023.

Cowin, S.C., 2001. Bone Mechanics Handbook. CRC press.

Damm, N.B., Morlock, M.M., Bishop, N.E., 2017. Influence of trabecular bone quality and implantation direction on press-fit mechanics. J. Orthop. Res. 35 (2), 224–233. https://doi.org/10.1002/jor.23257.

Dantas, T.A., Carneiro Neto, J.P., Alves, J.L., Vaz, P.C.S., Silva, F.S., 2020. In silico evaluation of the stress fields on the cortical bone surrounding dental implants: comparing root-analogue and screwed implants. J. Mech. Behav. Biomed. Mater. 104 (January), 103667. https://doi.org/10.1016/j.jmbbm.2020.103667.

Davies, J.E., 1996. In vitro modeling of the bone/implant interface. Anat. Rec. 245 (2), 426–445. https://doi.org/10.1002/(SICI)1097-0185(199606)245:2<426::AID-AR21>3.0.CO;2-Q.

Davies, J.E., 2003. Understanding peri-implant endosseous healing. J. Dent. Educ. 67 (8), 932–949. https://doi.org/10.1002/j.0022-0337.2003.67.8.tb03681.x.

Dragoni, E., 1994. Effect of thread shape on screw stress concentration by photoelastic measurements. J. Offshore Mech. Arctic Eng. 116 (4), 228–232. https://doi.org/10.1115/1.2920156.

Du, J., Lee, J.H., Jang, A.T., Gu, A., Hossaini-Zadeh, M., Prevost, R., Curtis, D.A., Ho, S. P., 2015. Biomechanics and strain mapping in bone as related to immediately-loaded dental implants. J. Biomech. 48 (12), 3486–3494. https://doi.org/10.1016/j.jbiomech.2015.05.014.

Fanali, S., Tumedei, M., Pignatelli, P., Inchingolo, F., Pennacchietti, P., Pace, G., Piattelli, A., 2021. Implant primary stability with an osteocondensation drilling protocol in different density polyurethane blocks. Comput. Methods Biomech. Biomed. Eng. 24 (1), 14–20. https://doi.org/10.1080/10255842.2020.1806251.

FEA manual guide. (n.d.). https://manuals.dianafea.com/d944/Analys/node405.html.

Ferreira, H., Mourão, C.F., Mello-Machado, R.C., Javid, K., dos Santos Pereira, R., Senna, P.M., 2023. Ex vivo analysis of ability of osseodensification to improve dental implant primary stability using xenograft bone walls. Appl. Sci. 13 (22). https://doi.org/10.3390/app132212337.

Fontes Pereira, J., Costa, R., Nunes Vasques, M., Salazar, F., Mendes, J.M., Infante da Câmara, M., 2023. Osseodensification: an alternative to conventional osteotomy in implant site preparation: a systematic review. J. Clin. Med. 12 (22). https://doi.org/10.3390/jcm12227046.

Gastal, E.S.L., Oliveiray, M.M., 2012. Adaptive manifolds for real-time high-dimensional filtering. ACM Trans. Graph. 31 (4), 1–13. https://doi.org/10.1145/2185520.2185529.

Goiato, M.C., Tonella, B.P., Ribeiro, P. do P., Ferraço, R., Pellizzer, E.P., 2009. Methods used for assessing stresses in buccomaxillary prostheses: photoelasticity, finite element technique, and extensometry. J. Craniofac. Surg. 20 (2). https://journals.lww.com/jcraniofacialsurgery/Fulltext/2009/03000/Methods_Used_for_Assessing_Stresses_in.66.aspx.

Guillaume, F., Le Cann, S., Tengattini, A., Törnquist, E., Falentin-Daudre, C., Albini Lomami, H., Petit, Y., Isaksson, H., Haïat, G., 2021. Neutron microtomography to investigate the bone-implant interface - comparison with histological analysis. Phys. Med. Biol. 66 (10). https://doi.org/10.1088/1361-6560/abf603.

Haraldson, T., 1980. A photoelastic study of some biomechanical factors affecting the anchorage of osseointegrated implants in the jaw. Scand. J. Plast. Reconstr. Surg. 14 (3), 209–214. https://doi.org/10.3109/02844318009106712.

He, T., Cao, C., Xu, Z., Li, G., Cao, H., Liu, X., Zhang, C., Dong, Y., 2017. A comparison of micro-CT and histomorphometry for evaluation of osseointegration of PEO-coated titanium implants in a rat model. Sci. Rep. 7 (1), 1–11. https://doi.org/10.1038/s41598-017-16465-4.

Hildebrand, T., Rüegsegger, P., 1997. A new method for the model-independent assessment of thickness in three-dimensional images. J. Microsc. 185 (1), 67–75. https://doi.org/10.1046/j.1365-2818.1997.1340694.x.

Holmes, D.C., Loftus, J.T., 1997. Influence of bone quality on stress distribution for endosseous implants. The Journal of Oral Implantology 23 (3), 104–111.

Hung, B.Q., Yu, W., Park, H.S., Kyung, H.M., Hong, M., 2022. Correlation between insertion torque and peri-implant bone strain during placement of orthodontic mini-implants: a finite element study. Am. J. Orthod. Dentofacial Orthop. 161 (2), 248–254. https://doi.org/10.1016/j.ajodo.2020.07.042.

Huwais, S., Meyer, E., 2017. A novel osseous densification approach in implant osteotomy preparation to increase biomechanical primary stability, bone mineral density, and bone-to-implant contact. Int. J. Oral Maxillofac. Implants 32 (1), 27–36. https://doi.org/10.11607/jomi.4817.

Isidor, F., 2006. Influence of forces on peri-implant bone. Clin. Oral Implants Res. 17 (Suppl. 2), 8–18. https://doi.org/10.1111/j.1600-0501.2006.01360.x.

Katranji, A., Misch, K., Wang, H.-L., 2007. Cortical bone thickness in dentate and edentulous human cadavers. J. Periodontol. 78 (5), 874–878. https://doi.org/10.1902/jop.2007.060342.

Kohli, N., Stoddart, J.C., van Arkel, R.J., 2021. The limit of tolerable micromotion for implant osseointegration: a systematic review. Sci. Rep. 11 (1), 1–11. https://doi.org/10.1038/s41598-021-90142-5.

Lahens, B., Neiva, R., Tovar, N., Alifarag, A.M., Jimbo, R., Bonfante, E.A., Bowers, M.M., Cuppini, M., Freitas, H., Witek, L., Coelho, P.G., 2016. Biomechanical and histologic basis of osseodensification drilling for endosteal implant placement in low density bone. An experimental study in sheep. J. Mech. Behav. Biomed. Mater. 63, 56–65. https://doi.org/10.1016/j.jmbbm.2016.06.007.

Lanyon, L., Rubin, C., 1985. Static vs dynamic loads as an influence on bone remodelling. J. Biomech. 18 (9), 729. https://doi.org/10.1016/0021-9290(85)90028-4.

Le Cann, S., Tudisco, E., Turunen, M.J., Patera, A., Mokso, R., Tägil, M., Belfrage, O., Hall, S.A., Isaksson, H., 2019. Investigating the mechanical characteristics of bone-metal implant interface using in situ synchrotron tomographic imaging. Front. Bioeng. Biotechnol. 6 (JAN). https://doi.org/10.3389/fbioe.2018.00208.

Lopez, C.D., Alifarag, A.M., Torroni, A., Tovar, N., Diaz-Siso, J.R., Witek, L., Rodriguez, E.D., Coelho, P.G., 2017. Osseodensification for enhancement of spinal surgical hardware fixation. J. Mech. Behav. Biomed. Mater. 69 (October 2016), 275–281. https://doi.org/10.1016/j.jmbbm.2017.01.020.

Meredith, N., 1998. Assessment of implant stability as a prognostic determinant. Int. J. Prosthod. 11 (5).

Merheb, J., Van Assche, N., Coucke, W., Jacobs, R., Naert, I., Quirynen, M., 2010. Relationship between cortical bone thickness or computerized tomography-derived bone density values and implant stability. Clin. Oral Implants Res. 21 (6), 612–617. https://doi.org/10.1111/j.1600-0501.2009.01880.x.

Mishra, A., 2020. Pelvic girdle ilium ischium and pubis. https://mishravetanatomy.blogspot.com/2020/03/Pelvic-Girdle-Ilium-Ischium-and-Pubis.html%0A.

Moncler, S.S., Salama, H., Reingewirtz, Y., Dubruille, J.H., 1997. Timing of loading and effect of micromotion on bone–dental implant interface: review of experimental literature. J. Biomed. Mater. Res. 43 (2), 192–203.

Otsu, N., 1979. A threshold selection method from gray-level histograms. In: IEEE Transactions on Systems, Man, and Cybernetics, vol. 9, pp. 62–66, 1.

Padhye, N.M., Padhye, A.M., Bhatavadekar, N.B., 2020. Osseodensification — A systematic review and qualitative analysis of published literature. Journal of Oral Biology and Craniofacial Research 10 (1), 375–380. https://doi.org/10.1016/j.jobcr.2019.10.002.

Park, S., Park, J., Kang, I., Lee, H., Noh, G., 2022. Effects of assessing the bone remodeling process in biomechanical finite element stability evaluations of dental implants. Comput. Methods Progr. Biomed. 221, 106852. https://doi.org/10.1016/j.cmpb.2022.106852.

Pearce, A.I., Richards, R.G., Milz, S., Schneider, E., Pearce, S.G., 2007. Animal models for implant biomaterial research in bone: a review. Eur. Cell. Mater. 13 (August 2020), 1–10. https://doi.org/10.22203/eCM.v013a01.

Porto, O.C.L., Silva, B.S. de F., Silva, J.A., Estrela, C.R. de A., de Alencar, A.H.G., Bueno, M.D.R., Estrela, C., 2020. CBCT assessment of bone thickness in maxillary and mandibular teeth: an anatomic study. J. Appl. Oral Sci. 28, 1–9. https://doi.org/10.1590/1678-7757-2019-0148.

Prendergast, P.J., Huiskes, R., Søballe, K., 1997. Biophysical stimuli on cells during tissue differentiation at implant interfaces. J. Biomech. 30 (6), 539–548. https://doi.org/10.1016/S0021-9290(96)00140-6.

Roux, S., Hild, F., Viot, P., Bernard, D., 2008. Three-dimensional image correlation from X-ray computed tomography of solid foam. Compos. Appl. Sci. Manuf. 39 (8), 1253–1265. https://doi.org/10.1016/j.compositesa.2007.11.011.

Ruffoni, D., Wirth, A.J., Steiner, J.A., Parkinson, I.H., Müller, R., van Lenthe, G.H., 2012. The different contributions of cortical and trabecular bone to implant anchorage in a

human vertebra. Bone 50 (3), 733–738. https://doi.org/10.1016/j.bone.2011.11.027.

Saidin, S., Abdul Kadir, M.R., Sulaiman, E., Abu Kasim, N.H., 2012. Effects of different implant-abutment connections on micromotion and stress distribution: prediction of microgap formation. J. Dent. 40 (6), 467–474. https://doi.org/10.1016/j.jdent.2012.02.009.

Schwarz, F., Herten, M., Sager, M., Wieland, M., Dard, M., Becker, J., 2007. Histological and immunohistochemical analysis of initial and early osseous integration at chemically modified and conventional SLA® titanium implants: preliminary results of a pilot study in dogs. Clin. Oral Implants Res. 18 (4), 481–488. https://doi.org/10.1111/j.1600-0501.2007.01341.x.

Sevimay, M., Turhan, F., Kiliçarslan, M.A., Eskitascioglu, G., 2005. Three-dimensional finite element analysis of the effect of different bone quality on stress distribution in an implant-supported crown. J. Prosthet. Dent 93 (3), 227–234. https://doi.org/10.1016/j.prosdent.2004.12.019.

Shah, F.A., Palmquist, A., 2017. Evidence that Osteocytes in Autogenous Bone Fragments can Repair Disrupted Canalicular Networks and Connect with Osteocytes in de novo Formed Bone on the Fragment Surface. Calcif. Tissue Int. 101 (3), 321–327. https://doi.org/10.1007/s00223-017-0283-2.

Sotto-Maior, B.S., Rocha, E.P., de Almeida, E.O., Freitas-Júnior, A.C., Anchieta, R.B., Del Bel Cury, A.A., 2010. Influence of high insertion torque on implant placement - an anisotropic bone stress analysis. Braz. Dent. J. 21 (6), 508–514. https://doi.org/10.1590/S0103-64402010000600005.

Steiner, J.A., Ferguson, S.J., van Lenthe, G.H., 2016. Screw insertion in trabecular bone causes peri-implant bone damage. Med. Eng. Phys. 38 (4), 417–422. https://doi.org/10.1016/j.medengphy.2016.01.006.

Taillandier-Thomas, T., Roux, S., Morgeneyer, T.F., Hild, F., 2014. Localized strain field measurement on laminography data with mechanical regularization. Nuclear Instruments and Methods in Physics Research, Section B: Beam Interactions with Materials and Atoms 324, 70–79. https://doi.org/10.1016/j.nimb.2013.09.033.

Trisi, P., Berardini, M., Falco, A., Podaliri Vulpiani, M., 2016. New osseodensification implant site preparation method to increase bone density in low-density bone: in vivo evaluation in sheep. Implant Dent. 25 (1), 24–31. https://doi.org/10.1097/ID.0000000000000358.

Trisi, P., Perfetti, G., Baldoni, E., Berardi, D., Colagiovanni, M., Scogna, G., 2009. Implant micromotion is related to peak insertion torque and bone density. Clin. Oral Implants Res. 20 (5), 467–471. https://doi.org/10.1111/j.1600-0501.2008.01679.x.

Turcio, K.H.L., Goiato, M.C., Filho, H.G., dos Santos, D.M., 2009. Photoelastic analysis of stress distribution in oral rehabilitation. J. Craniofac. Surg. 20 (2). https://journals.lww.com/jcraniofacialsurgery/Fulltext/2009/03000/Photoelastic_Analysis_of_Stress_Distribution_in.44.aspx.

Udomsawat, C., Rungsiyakull, P., Rungsiyakull, C., Khongkhunthian, P., 2019. Comparative study of stress characteristics in surrounding bone during insertion of dental implants of three different thread designs: a three-dimensional dynamic finite element study. Clinical and Experimental Dental Research 5 (1), 26–37. https://doi.org/10.1002/cre2.152.

Verbruggen, S.W., Vaughan, T.J., McNamara, L.M., 2012. Strain amplification in bone mechanobiology: a computational investigation of the in vivo mechanics of osteocytes. Journal of the Royal Society Interface 9 (75), 2735–2744. https://doi.org/10.1098/rsif.2012.0286.

Walid, M.A., Almutairi, A.S., Alkhodary, M.A., 2019. The effect of osseodensification and different thread designs on the dental implant primary stability [version 1 ; peer review : 2 approved , 1 approved with reservations] Abdullah Saleh Almutairi Referee Status. F1000Research 1–10. May.

Wili, P., Rauber, C., Saade, A., Bliggenstorfer, S., Ramirez-Garmendia, V., Schweizer, R., Irastorza-Landa, A., Chappuis, V., Zysset, P., 2024. Primary stability of dental implants in human jawbones: experiments & FE analyses. Clin. Oral Implants Res. 1–14. https://doi.org/10.1111/clr.14386.

Yang, B., Irastorza-Landa, A., Heuberger, P., Ploeg, H.-L., 2023. Digital Image Correlation Validation of Finite Element Strain Analysis of Dental Implant Insertion for Two Implant Designs, pp. 1–10. https://doi.org/10.1115/VVUQ2023-107659.

Zhou, Y., Gong, C., Hossaini-Zadeh, M., Du, J., 2020. 3D full-field strain in bone-implant and bone-tooth constructs and their morphological influential factors. J. Mech. Behav. Biomed. Mater. 110 (March), 103858. https://doi.org/10.1016/j.jmbbm.2020.103858.